Journal of Applied Mechanics and Technical Physics, Vol. 51, No. 4, pp. 555–568, 2010

MESOMECHANICS OF MATERIAL STRENGTHENING BY NANODISPERSE INCLUSIONS

V. E. Panin, E. E. Deryugin, and S. N. Kul'kov

UDC 69.4, 539.376, 539.4.015

By simultaneously using approaches of mesomechanics and nonequilibrium thermodynamics, it is shown that any nanoinclusions, including those with a low elastic modulus, and nanopores cause material strengthening.

Key words: *mesomechanics, nonequilibrium thermodynamics, stress concentration, nanosize inclusions, nanopores, grain boundary, gradients of elastic constants.*

INTRODUCTION

The loading curve of materials with inclusions is influenced by various factors. It is expected that the qualitative and quantitative characteristics of stress–strain curves depend not only on the type of particles but also on their sizes.

Initiation and motion of deformation defects at any scale level are due primarily to local structural transformations in regions of increased stress concentration [1]. It is therefore very important to characterize any inclusion in a deformable solid body by the spatial distribution of the stress field produced by this inclusion.

In the present paper, a possible strengthening mechanism for materials containing nanosize inclusions with elastic moduli smaller than that of their surrounding matrix is analyzed using a multilevel approach based on the physical mesomechanics of materials. For materials of the type considered, the internal stress fields around nanoinclusions are calculated using the relaxation element method [2] and the thermodynamic foundations of the theory of strengthening of materials with nanosize inclusions having low elastic moduli, including materials with nanopores, are considered.

1. STRESS FIELD IN A MATRIX WITH A NANOSIZE INCLUSION

1.1. Analytical Formulas for the Stress Field in a Plate with an Inclusion. Below, we give the results of two-dimensional calculations of the stress fields in an elastic matrix with a round inclusion in tension under plane stress conditions using the relaxation element method [2]. It is assumed that the elastic characteristics of the matrix and inclusion materials are different: E_1 and ν_1 are the Young modulus and Poisson ratio of the matrix, respectively, and E_2 and ν_2 are the Young modulus and Poisson ratio of the inclusion, respectively. The tension stress σ is directed along the y cartesian axis with origin at the center of the inclusion.

To solve this problem, it is necessary to determine the boundary conditions on the inclusion contour. The loading diagram is presented in Fig. 1a.

Institute of Strength Physics and Materials Science, Siberian Division of the Russian Academy of Sciences, Tomsk 634021; Tekhnicheskaya Fizika, Vol. 51, No. 4, pp. 127–142, July–August, 2010. Original article submitted April 22, 2010.

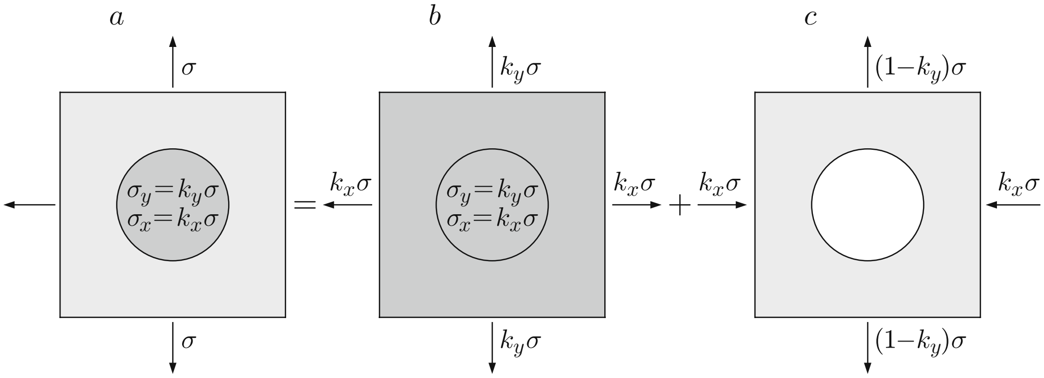

Fig. 1. Boundary conditions represented as a superposition of the stress fields: (a) stress field in the plate with an inclusion; (b) homogeneous biaxial stress field; (c) stress field under biaxial loading provided that the stresses in the local region of round shape are equal to zero.

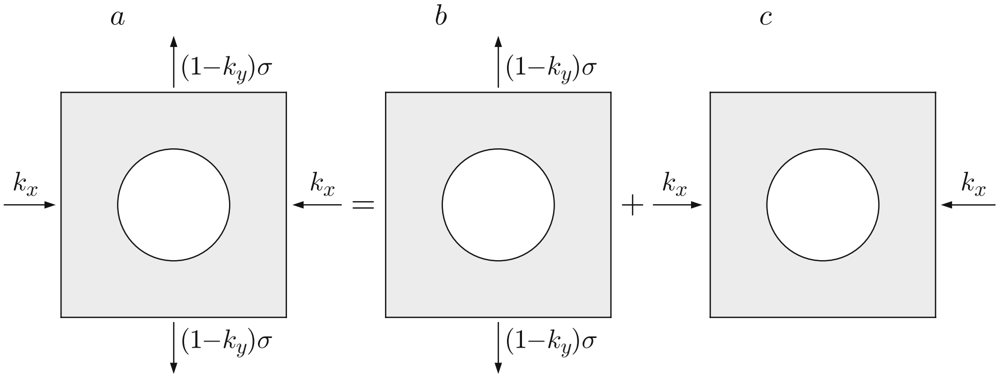

Fig. 2. Biaxial loading of the plate (a) represented as a superposition of two uniaxial loads along the y axe (b) and x axe (c).

It has been shown [3, 4] that in an elliptic inclusion symmetric about the tension axis, the stress field is homogeneous with the zero component σ_{xy}. Hence, this field is also homogeneous in the case of an inclusion of round shape. The field in the inclusion will be characterized by the components

$$\sigma_y^0 = k_y\sigma, \qquad \sigma_x^0 = k_x\sigma, \tag{1}$$

where the coefficients k_y and k_x are to be determined.

Let us use the superposition principle which is valid in the approximation of linear elastic theory. According to this principle, the total solution of the boundary-value linear problem of elasticity can be represented as a superposition of simpler solutions provided that the resulting boundary conditions remain former. Figure 1 shows a combination of two simple solutions which do not disturb the initial boundary conditions. One of these solutions is the homogeneous stress field (1) (see Fig. 1b), which defines a homogeneous elastic-strain field with the components

$$\varepsilon_y = (k_y - \nu_1 k_x)\sigma/E_1, \qquad \varepsilon_x = (k_x - \nu_1 k_y)\sigma/E_1, \qquad \varepsilon_{xy} = 0. \tag{2}$$

The second solution is the solution in the case of a plate subjected to biaxial external loading (see Fig. 1c) provided that the stress in the inclusion is equal to zero. This solution, in turn, can be represented as a superposition of two solutions for uniaxial load that satisfy the boundary conditions specified in Fig. 1c (Fig. 2). In the case of uniaxial loading of a plate with a circular region without normal and tangential stress on its boundary, the solution is the well-known Kirsch solution [5–8]. Using this solution, one can find the inhomogeneous stress field σ^* outside the circular contour for the case of tension stress $\sigma(1 - k_y)$ (Fig. 2b). The stress field σ^{**} for the case of external compression stress σk_x (Fig. 2c) is similarly determined. Superposition of the obtained solutions, together with the homogeneous field (1), defines the stress field outside the inclusion with the components

$$\frac{\sigma_y}{\sigma} = 1 + \frac{(1-k_y+k_x)R^2}{2r^2}\Big[3\Big(1-\frac{2y^2}{r^2}\Big) + \Big(1-\frac{8y^2x^2}{r^4}\Big)\Big(\frac{3R^2}{r^2}-2\Big)\Big] - \frac{k_xR^2}{r^2}\Big(1-\frac{2y^2}{r^2}\Big),$$

$$\frac{\sigma_x}{\sigma} = \frac{(1-k_y+k_x)R^2}{2r^2}\Big[\Big(1-\frac{2y^2}{r^2}\Big) - \Big(1-\frac{8y^2x^2}{r^4}\Big)\Big(\frac{3R^2}{r^2}-2\Big)\Big] + \frac{k_xR^2}{r^2}\Big(1-\frac{2y^2}{r^2}\Big), \tag{3}$$

$$\frac{\sigma_{xy}}{\sigma} = \frac{(1-k_y-k_x)R^2yx}{r^4}\Big(3-\frac{2(3R^2+4y^2)}{r^2}+\frac{12R^2y^2}{r^4}\Big) - \frac{2k_yR^2yx}{r^4}.$$

It is obvious that inside the inclusion, the following stress distribution is valid:

$$\sigma_y/\sigma = k_y, \qquad \sigma_x/\sigma = k_x, \qquad \sigma_{xy}/\sigma = 0.$$

Displacements of an arbitrary point (x_0, y_0) on the boundary of the inclusion subject to the boundary conditions in Fig. 2b and c are given by the equations

$$u_y^*(x_0,y_0) = 3(1-k_y)y_0\sigma/E_1, \qquad u_x^*(x_0,y_0) = -(1-k_y)x_0\sigma/E_1,$$
$$u_y^{**}(x_0,y_0) = k_xy_0\sigma/E_1, \qquad u_x^{**}(x_0,y_0) = -3k_xx_0\sigma/E_1. \tag{4}$$

The components of the additional displacements u_y^0 and u_x^0 of this point (x_0, y_0) due to the homogeneous stress field (1) are determined by the homogeneous strain field (2):

$$u_y^0(x_0,y_0) = y_0(k_y - k_x\nu_1)\sigma/E_1, \qquad u_x^0(x_0,y_0) = x_0(k_x - k_y\nu_1)\sigma/E_1. \tag{5}$$

The displacement of an arbitrary point (x_0, y_0) on the boundary of the inclusion is determined by summation of the corresponding components in Eqs. (4) and (5):

$$u_x(x_0,y_0) = u_x^0(x_0,y_0) + u_x^*(x_0,y_0) + u_x^{**}(x_0,y_0),$$
$$u_y(x_0,y_0) = u_y^0(x_0,y_0) + u_y^*(x_0,y_0) + u_y^{**}(x_0,y_0). \tag{6}$$

It is easy to show that condition (6) is satisfied for a homogeneous strain field with the components

$$\varepsilon_x = -[1+2k_x-k_y(1-\nu_1)]\sigma/E_1, \qquad \varepsilon_y = [3-2k_y+k_x(1-\nu_1)]\sigma/E_1, \qquad \varepsilon_{xy} = 0, \tag{7}$$

where k_y, k_x are unknown coefficients.

At the same time, the homogeneous stress field (1) in the inclusion (see Fig. 1b) corresponds to homogeneous deformation which can be expressed in terms of the elastic characteristics of the inclusion:

$$\varepsilon_x = (k_x - k_y\nu_2)\sigma/E_2, \qquad \varepsilon_y = (k_y - k_x\nu_2)\sigma/E_2, \qquad \varepsilon_{xy} = 0. \tag{8}$$

Equating the corresponding components in expressions (7) and (8), we obtain a system of two equations with two unknowns k_y and k_x which can be written as

$$k_y(E_1+2E_2) - k_x[\nu_2E_1 + (1-\nu_1)E_2] = 3E_2, \qquad k_x(E_1+2E_2) - k_y[\nu_2E_1+(1-\nu_1)E_2] = -E_2.$$

The solution of this system gives the values of the coefficients k_y and k_x:

$$k_y = \frac{E_2[(3-\nu_2)E_1 + (5+\nu_1)E_2]}{(E_1+2E_2)^2 - [\nu_2E_1+(1-\nu_1)E_2]^2}, \quad k_x = \frac{E_2[(3\nu_2-1)E_1+(1-3\nu_1)E_2]}{(E_1+2E_2)^2-[\nu_2E_1+(1-\nu_1)E_2]^2}. \tag{9}$$

The obtained equations (3) and (9) coincide with the equations in [9] found by selection of certain stress functions, which confirms the validity of these equations.

Plastic deformation occurs under shear stress relaxation conditions. In a matrix without inclusions under external stress σ, any point is exposed the maximum shear stress $\tau_0 = 0.5\sigma$ at an angle of 45° to the tension axis. Simple transformations of expressions (3) outside the inclusion yield the following distribution of the shear stress $\tau = (\sigma_y - \sigma_x)/2$ at an angle of 45° to the tension axis:

$$\tau = \frac{1}{2}\sigma + \frac{(1-k_y+k_x)R^2\sigma}{2r^2}\Big(1-8\frac{x^2y^2}{r^4}\Big)\Big(\frac{3R^2}{r^2}-2\Big) + \frac{(1-k_y-k_x)R^2\sigma}{2r^2}\Big(1-\frac{2y^2}{r^2}\Big). \tag{10}$$

In the inclusion, $\tau = (k_y - k_x)/2$.

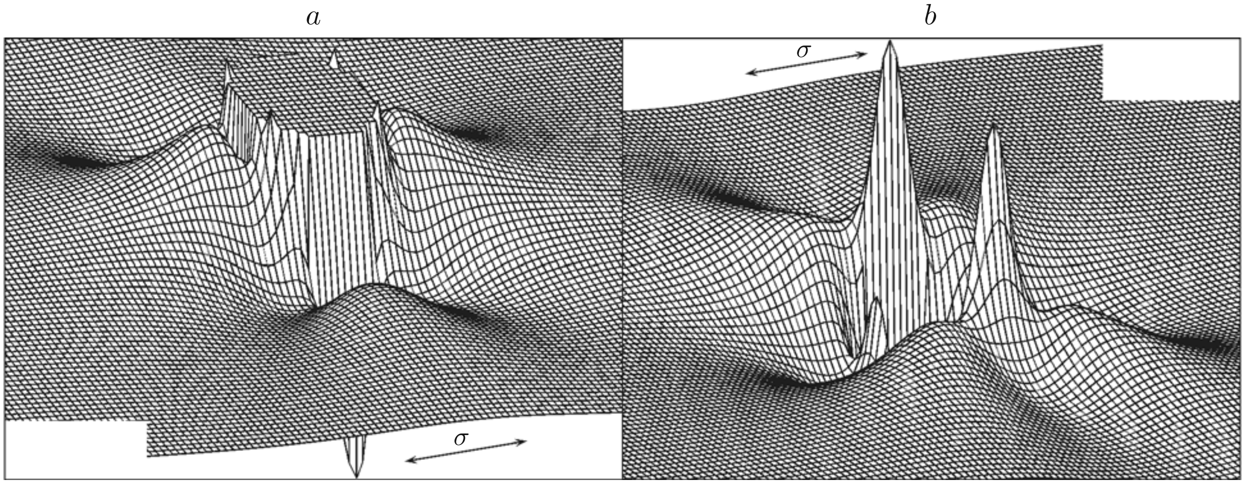

Fig. 3. Distributions of the shear stress τ at an angle 45° to the tension axis: (a) hard inclusion ($\tau_{\max}/\sigma = 0.709$ and $\tau_{\min}/\sigma = 0.122$); (b) soft inclusion ($\tau_{\max}/\sigma = 0.67$ and $\tau_{\min}/\sigma = 0.38$).

Figure 3 gives shear stress distributions in the presence of hard and soft inclusions.

In a hard inclusion (titanium carbide with $E_2 = 382$ GPa, $\nu_2 = 0.3$ in iron with $E_1 = 190$ GPa and $\nu_1 = 0.28$ [10]) a homogeneous field of the shear stress $\tau = 0.683\sigma$ is observed whose value far exceeds the homogeneous field of the shear stress $\tau_0 = 0.5\sigma$ in the iron matrix without inclusions. In this case, near the inclusion boundary in the matrix there are four maxima $\tau_{\max} = 0.709\sigma$. In addition, there are two regions with increased shear stress, in which the maximum stress is $\tau_{\max} = 0.643\sigma$. In addition, near the inclusion boundary in the matrix there are two minima $\tau_{\min} = 0.122\sigma$, which are far smaller than the values of τ_0.

A different pattern is observed in the case of a soft inclusion in a harder matrix (for example, copper sulfide CuS in iron). The minimum stress $\tau_{\min} = 0.384\sigma$ is observed in the inclusion. Near the inclusion boundary there are two maxima $\tau_{\max} = 0.67\sigma$. The stress distribution outside the soft inclusion is qualitatively similar to the stress distribution in a matrix with a circular cut [8].

The analysis performed above shows that in all the cases considered, the large inclusion acts as a stress macroconcentrator. The jump in the elastic constants on the inclusion boundary is responsible for softening of the material. The stress concentration will be even greater if the particle has an irregular (asymmetric) shape [11].

1.2. Stress Field in a Matrix with Nanosize Particles. The nanosize elements of the structure have indistinct boundaries (transition region whose width is comparable to the size of the particle itself) [12–15]. Therefore, in calculations of the stress field in a matrix with a nanosize particle, it is necessary to take into account the gradients of the elastic constants across the nanoparticle–matrix interface. The present paper gives the results of calculations taking into account a smooth change (in the transition region) in the elastic moduli from their values in the matrix to the values in the nanoparticle. Zeroth elastic constants in the nanoparticle correspond to the case of a material with nanopores.

Let h be the width of the transition region in which the Young modulus decreases from the value E_1 in the matrix to the value E_2 in the nanoparticle. In the transition region, a gradient of the elastic moduli is observed. We assume that, generally, the Young modulus in the transition region has an S-shaped shape profile (Fig. 4), which provides smooth transition from the value E_1 in the matrix to the value E_2 in the nanoparticle.

The smooth change in the Young modulus in the transition region is given by the formula

$$E(r) = (1 - g/h)E^1(r) + (g/h)E^2(r); \tag{11}$$

$$E^1(r) = E_1 + (E_2 - E_1)\Big(1 - \frac{R - g - r}{h - g}\Big)^{\beta+1}, \qquad R - h \leqslant r \leqslant R - g; \tag{12}$$

$$E^2(r) = E_1 + (E_2 - E_1)\Big(\frac{R - r}{g}\Big)^{\beta+1}, \qquad R - g \leqslant r \leqslant R, \tag{13}$$

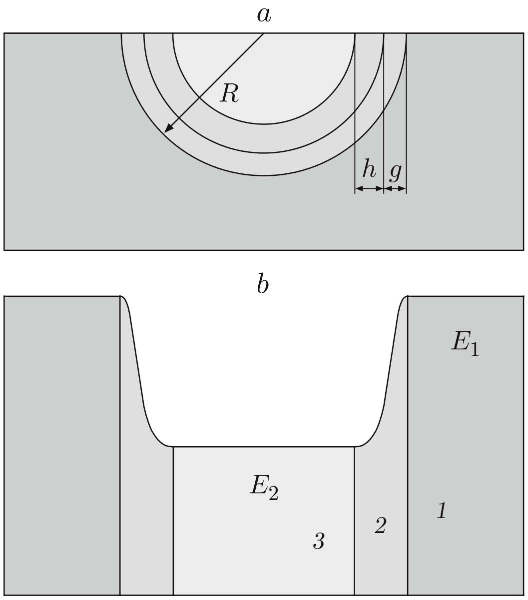

Fig. 4. Diagram of half of the nanoinclusion (a) and Young modulus profile (b) in the radial section of the soft nanoinclusion: 1) matrix; 2) transition region; 3) nanoinclusion.

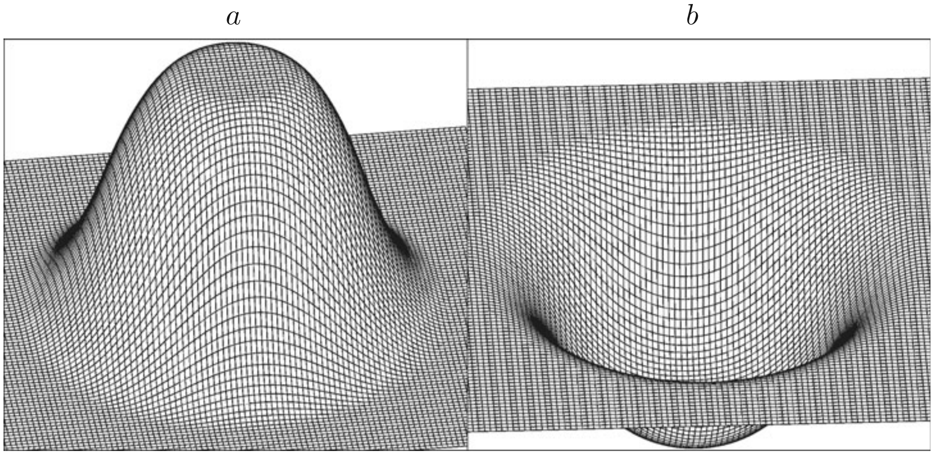

Fig. 5. Distribution of the Young modulus in hard nanoparticle (a) and soft nanoparticle (b).

where R is the nanoparticle radius (taking into account the width of the boundary), $R - g$ is the distance from the center of the nanoparticle to the site in the transition region at which the maximum gradient of the Young modulus is observed; the exponent β determines the gradient of the Young modulus in the transition region: the larger the β, the larger the maximum gradient of the Young modulus. In the limiting case ($\beta \to \infty$), a jump in the Young modulus is observed on the inclusion boundary. In this case, the size of the inclusion is determined by the quantity $R - g$.

Figure 5 shows distributions of the Young modulus calculated by formula (11) for the two cases: a hard nanoparticle of titanium carbide TiC ($E_2 = 484$ GPa [10]) and a soft nanoparticle copper sulfide CuS in iron ($E_1 = 195$ GPa [10]) for $\beta = 1$, $h = 0.8R$, and $g = 0.5h$. It was assumed that the Young modulus of the CuS nanoparticle did not exceed the value for annealed copper ($E_2 = 110$ GPa [10]). Figure 6 shows Young modulus profiles in the radial section of the nanoparticle for $h = R$. It is evident that the Young modulus distribution according to formulas (11)–(13) does not have jumps during transition from the matrix to the nanoparticle.

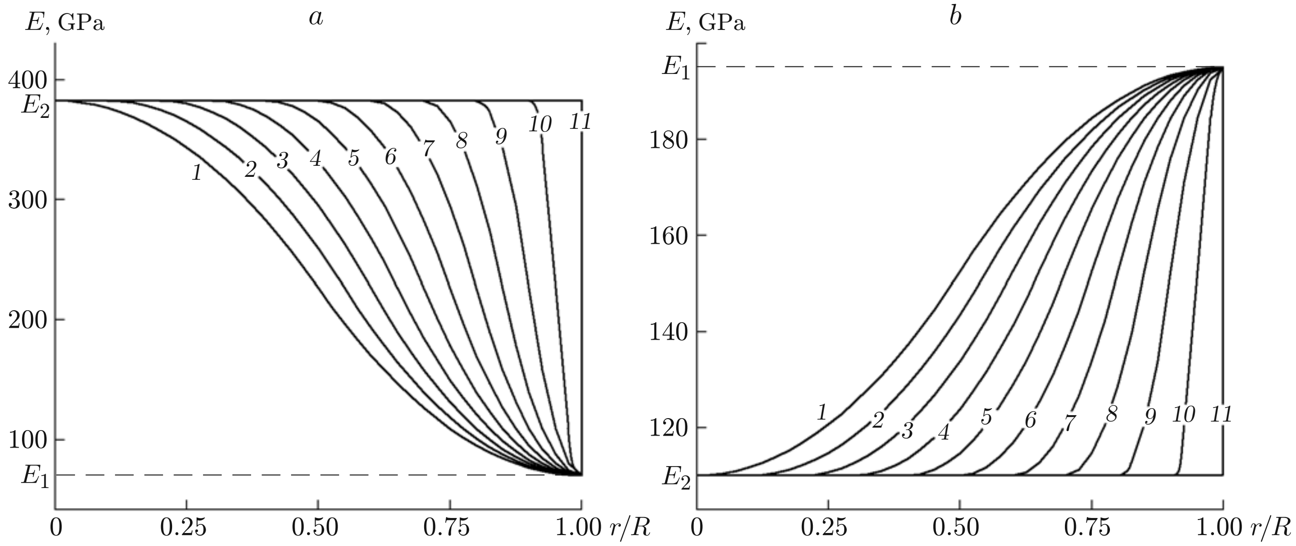

Fig. 6. Young modulus profiles in the radial section of hard nanoparticle (a) and soft nanoparticle (b) for $g = 0.5h$ and and different values of β in Eqs. (12) and (13): $\beta = 1$ (1), 2 (2), 3 (3), 4 (4), 5 (5), 6 (6), 7 (7), 8 (8), 9 (9), 10 (10), and ∞ (11): (a) $E_1 = 70$ GPa and $E_2 = 382$ GPa; (b) $E_1 = 195$ GPa and $E_2 = 110$ GPa.

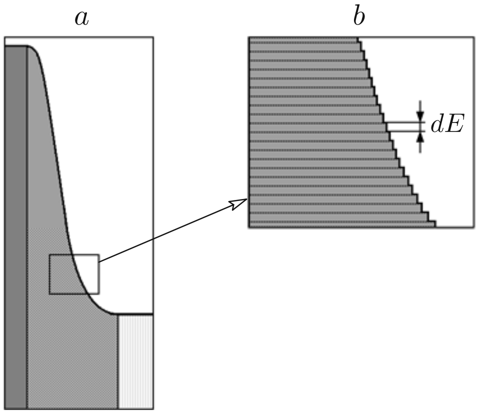

Fig. 7. Fragment of the smooth Young modulus profile E (a) and the site of this profile represented as elementary jumps dE (b) in the transition region.

It is convenient to represent Eqs. (12) and (13) as a function of the variables t' and t'' [$t' = (R-g-r)/(h-g)$ in the interval $R-h \leqslant r \leqslant R-g$ and $t'' = (R-r)/g$ in the interval $R-g \leqslant r \leqslant R$]. Then, these equations can be written as

$$E^1(t') = E_1 + (E_2 - E_1)(1-t')^{\beta+1}, \qquad E^2(t'') = E_1 + (E_2 - E_1)(t'')^{\beta+1}. \tag{14}$$

Poisson ratios are determined similarly in the corresponding intervals:

$$\nu^1(t') = \nu_1 + (\nu_2 - \nu_1)(1-t')^{\beta+1}, \qquad \nu^2(t'') = \nu_1 + (\nu_2 - \nu_1)(t'')^{\beta+1}. \tag{15}$$

To calculate the stress state of a matrix with nanoinclusions (taking into account gradients of the elastic moduli in the transition region), we represent the continuous change in the moduli in the transition region (Fig. 7a) as a set of infinitesimal jumps (Fig. 7b).

The elementary jumps of the Young modulus (Fig. 7b) and Poisson ratio are given by the first derivatives of expressions (14) and (15) with respect to the corresponding variables. In the interval $R-h \leqslant r \leqslant R-g$, we obtain

$$dE' = (\beta+1)(E_2 - E_1)(1-t')^{\beta}\, dt', \qquad d\nu' = (\beta+1)(\nu_2 - \nu_1)(1-t')^{\beta}\, dt'.$$

In the interval $R-g \leqslant r \leqslant R$, the corresponding elementary jumps of the Young modulus are given by

$$dE'' = (\beta+1)(E_2-E_1)(t'')^\beta\, dt'', \qquad d\nu'' = (\beta+1)(\nu_2-\nu_1)(t'')^\beta\, dt''.$$

The variables t' and t'' in the corresponding transition regions vary from 0 to 1 in the direction to the center of the nanoparticle.

Each elementary jump of the elastic moduli determines the elementary field of shear stresses, which, according to expression (10), can be represented as

$$d\tau = \frac{R(t)^2}{2r^2}\Big(1-8\,\frac{x^2y^2}{r^4}\Big)\Big(\frac{3R(t)^2}{r^2}-2\Big)\,dk_1 + \frac{R(t)^2}{2r^2}\Big(1-\frac{2y^2}{r^2}\Big)\,dk_2. \tag{16}$$

In this expression, the coefficients dk_1 and dk_2 and the radius of the circular contour on which there is an elementary jump of the elastic moduli $R(t)$ are functions of the variable t' in the interval $R-h \leqslant r \leqslant R-g$ and the variable t'' in the interval $R-g \leqslant r \leqslant R$. The corresponding calculations give the following equations for dk_1 and dk_2:

— in the interval $R-h \leqslant r \leqslant R-g$,

$$dk_1' = \frac{(\beta+1)(1-t')^\beta[E_1(1+\nu_2)-E_2(1+\nu_1)]}{4[E_1+(E_2-E_1)(1-t')^\beta]}\,dt',$$

$$dk_2' = \frac{(\beta+1)(1-t')^\beta[E_1(1-\nu_2)-E_2(1-\nu_1)]}{2[E_1+(E_2-E_1)(1-t')^\beta]}\,dt';$$

— in the interval $R-g \leqslant r \leqslant R$,

$$dk_1'' = \frac{(\beta+1)(t'')^\beta[E_1(1+\nu_2)-E_2(1+\nu_1)]}{4[E_1+(E_2-E_1)(t'')^\beta]}\,dt'',$$

$$dk_2'' = \frac{(\beta+1)(t'')^\beta[E_1(1-\nu_2)-E_2(1-\nu_1)]}{2[E_1+(E_2-E_1)(1-t'')^\beta]}\,dt''.$$

Substitution of these values into Eq. (16) and integration in the corresponding limits lead to the following shear-stress distribution in the volume:

$$\tau(r,\beta) = \tau_1(r,\beta)(1-g/h) + \tau_2(r,\beta)(g/h).$$

In the interval $R-h \leqslant r$, the function $\tau_1(r,\beta)$ has the form

$$\tau_1(r,\beta) = A^1(r) + 0.5[1-B^1(r)] + \frac{1-B^1(r)}{4(\beta+1)^{-1}}\Big[\frac{E_1(1+\nu_2)-E_2(1+\nu_1)}{2r^2}\Big(1-8\,\frac{x^2y^2}{r^4}\Big)$$

$$\times \int\limits_{B^1(r)}^{1} \frac{\{3[R-g-t(h-g)]^2-2r^2\}[R-g-t(h-g)]^2}{r^2\{E_1+(E_2-E_1)[1-(1-t)^{\beta+1}]\}(1-t)^{-\beta}}\,dt$$

$$+ \frac{E_1(1-\nu_2)-E_2(1-\nu_1)}{r^2}\Big(1-\frac{2y^2}{r^2}\Big)\int\limits_{B^1(r)}^{1}\frac{[R-g-t(h-g)]^2(1-t)^\beta}{E_1+(E_2-E_1)[1-(1-t)^{\beta+1}]}\,dt\Big].$$

Here $B^1(r) = (R-g-r)/(h-g)$ and $A^1(r) = B^1(r)(k_y-k_x)/2$ at $R-h \leqslant r \leqslant R-g$; $B^1(r) = A^1(r) = 0$ at $r \geqslant R-g$. In the interval $r \leqslant R-h$, we have $\tau_2(r,\beta) = (k_y-k_x)/2$, where k_y and k_x are given by Eqs. (9).

In the interval $R-g \leqslant r$, the function $\tau_2(r,\beta)$ has the form

$$\tau_2(r,\beta) = A^2(r)+0.5[1-B^2(r)]+\frac{1-B^2(r)}{4(\beta+1)^{-1}}\Big[\frac{E_1(1+\nu_2)-E_2(1+\nu_1)}{2r^2}\Big(1-8\,\frac{x^2y^2}{r^4}\Big)\int\limits_{B^2(r)}^{1}\frac{[3(R-tg)^2-2r^2](R-tg)^2}{r^2[E_1+(E_2-E_1)t^{\beta+1}]t^{-\beta}}\,dt$$

$$+ \frac{E_1(1-\nu_2)-E_2(1-\nu_1)}{r^2}\Big(1-\frac{2y^2}{r^2}\Big)\int\limits_{B^2(r)}^{1}\frac{(R-tg)^2t^\beta}{E_1+(E_2-E_1)t^{\beta+1}}\,dt\Big],$$

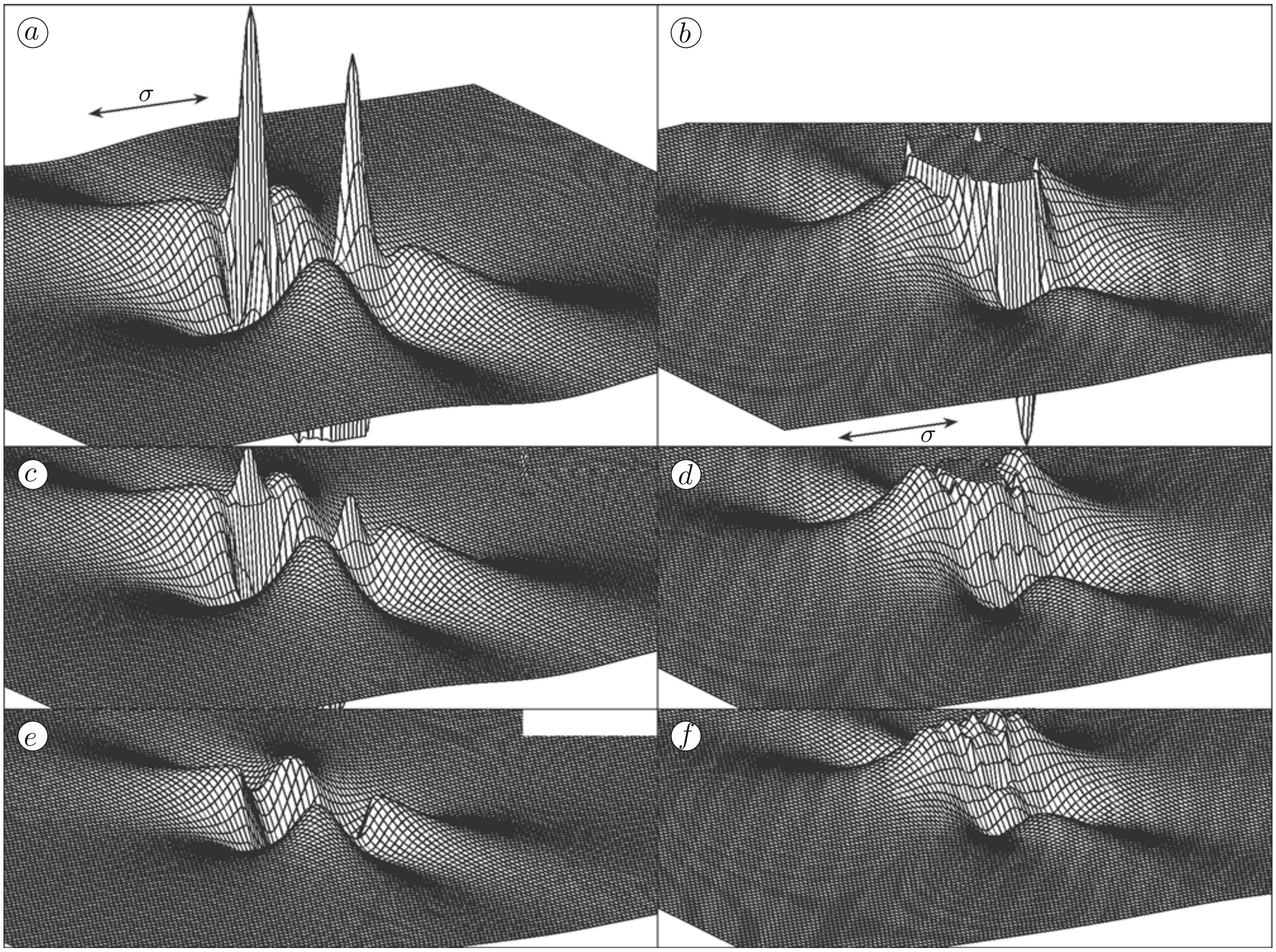

Fig. 8. Variation in the shear stress distribution around a CuS soft inclusion (a, c, and e) and a TiC hard inclusion (b, d, and f) in an iron matrix with decreasing radius of the inclusion: $R > 10$ μm (a and b), 33 nm (c), 20 nm (d), and 10 nm (e and f).

where $B^2(r) = (R - r)/g$ and $A^2(r) = B^2(r)(k_y - k_x)/2$ at $R - g \leqslant r \leqslant R$; $B^2(r) = A^2(r) = 0$ at $r \geqslant R$. In the interval $r \leqslant R - g$, we have $\tau_2(r, \beta) = (k_y - k_x)/2$, where k_y and k_x are given by Eqs. (9).

The calculations show that the stress concentration around the inclusion decreases with decreasing size of the inclusion relative to the width of the transition region. Figure 8 shows the variation in the field of the maximum spall stress τ as the radius of the soft inclusion decreases from 10 μm to 10 nm. It is evident that large inclusion acts as a strong stress concentrator whereas near the boundary of the nanoinclusions, the stress concentration is insignificant.

The change in the Young modulus in transition from the matrix to the inclusion is due to the continuous change in the bulk-centered cubic crystal structure of iron to the face-centered cubic crystal structure of CuS ($E_2 = 110$ GPa) in the transition region. In other words, the width of the transition region is the effective length scale at which the Young modulus gradient takes place. The Poisson ratio changes similarly in the transition from the iron matrix to the CuS inclusion. The width of the transition region was assumed to be independent of the size of the inclusion.

A comparison of the distributions of the stress τ for a soft inclusion (Fig. 8a, c, and e) and a hard inclusion (Fig. 8b, d , and f) shows that they differ qualitatively. However, in the case of a TiC hard inclusion ($E_2 = 484$ GPa [9]) in an iron matrix, the stress concentration around the inclusion decreases with decreasing size of the inclusion. In both cases, the distribution pattern changes qualitatively when the influence of the inclusion boundary extends to a distance exceeding half of the inclusion radius.

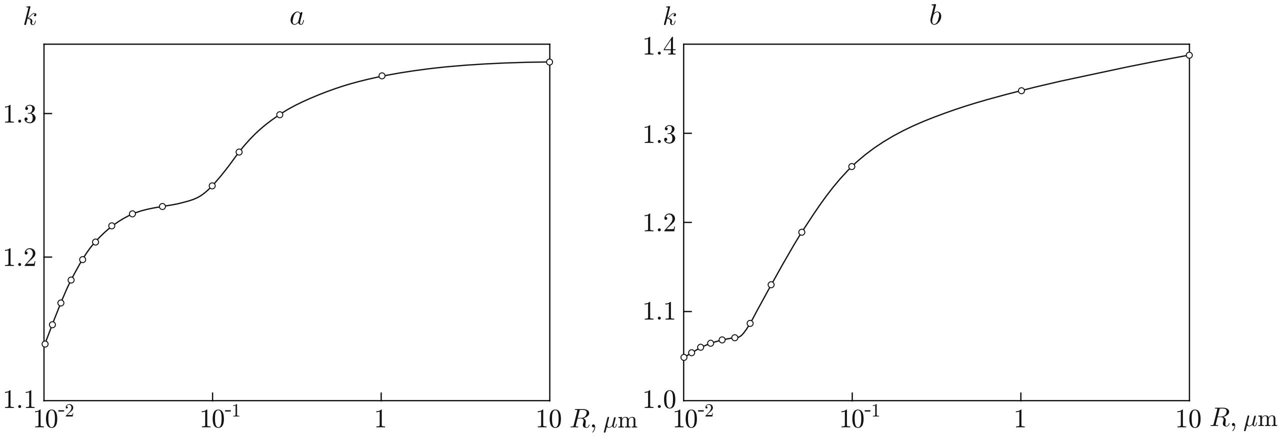

Fig. 9. Shear stress concentration coefficient versus radius of a CuS soft inclusion (a) and a TiC hard inclusion (b) in an iron matrix.

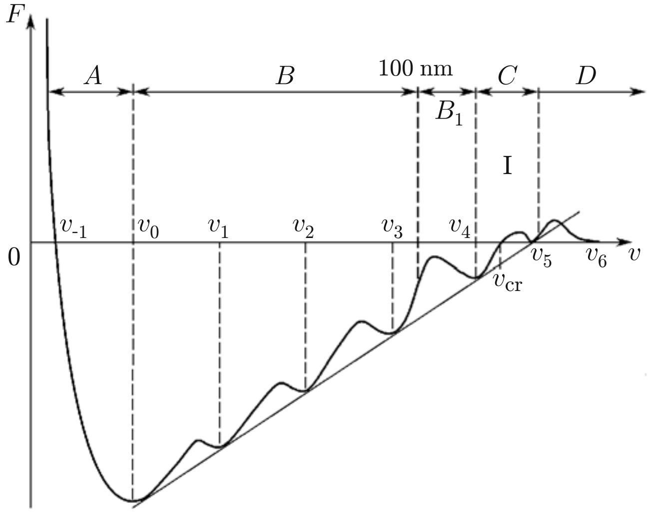

Fig. 10. Gibbs thermodynamic potential F versus molar volume v: A is the region of hydrostatic compression, B is the region of mesostructures of various scale levels, B_1 and C are the regions of nanosize structures, D is the region of transition of the material to the porous state and fracture; and I is the region corresponding to the strongly nonequilibrium transition state.

Figure 9 gives the shear stress concentration coefficient k versus radius R for hard and soft inclusions. It is evident that in the range of large sizes of the hard and soft inclusions, the stress concentration gradients are similar, whereas in the range of nanosizes, they differ significantly: $\operatorname{grad} k$ is 2.5 times larger for the hard inclusion than for the soft inclusion. A dislocation should bend around a hard nanoinclusion according the Orovan model [16], whereas the soft nanoinclusion is cut through by the dislocation. Below, we show that in the case of soft nanoinclusions, strengthening rather than softening of the material occurs.

2. NONEQUILIBRIUM THERMODYNAMICS OF MATERIAL STRENGTHENING BY INTRODUCING SOFT NANOINCLUSIONS AND NANOPORES

Figure 10 shows a curve of the Gibbs thermodynamic potential F versus molar volume v. For the critical values of the molar volume v_i $(i = 1, 2, \ldots, 6)$, the thermodynamic potential $F(v_i)$ has local minima corresponding to the local nonequilibrium potentials in the zones of hydrostatic tension of various scales. The critical values of v_i correspond to the following states in the deformable solid body: v_0 is the equilibrium crystal, v_1 are the regions of

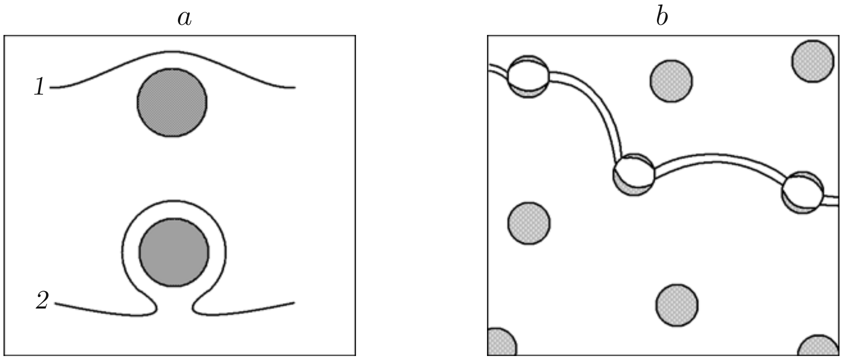

Fig. 11. Dislocation motion: (a) interaction of a dislocation with a disperse inclusion according to the Orovan model [approach of a dislocation to a high-strength inclusion (curve 1), formation of a dislocation loop near an inclusion (curve 2)]; (b) passage of a dislocation through a nanoinclusion with a small elastic modulus.

stress microconcentrators in which dislocation nuclei occur, v_2 and v_3 are the regions of stress mesoconcentrators and macroconcentrators in which local structural-phase transitions occur with the formation of mesozones and macrozones of localized plastic deformation, respectively, and v_4 is the state corresponding to the intersection of the curve of $F(v)$ with the abscissa [with a further increase in the local molar volume, the change in the Gibbs thermodynamic potential occurs under the conditions $F(v) > 0$; in this case, the system becomes unstable: various types of fracture occur in the material]; for $v > v_4$, two phases coexist: an atom-vacancy phase (at $v = v_5$) and local vacuum (at $v \geqslant v_6$) in the form of micropores, defects, and discontinuities.

From Fig. 10, it follows that all local minima of the curve of $F(v)$ have common conodes with the main minimum of the equilibrium thermodynamic potential for $v = v_0$. This implies that a deformable solid with localized plastic flow should always have an undeformed equilibrium medium, in which all types of deformation defects, including unstable atom-vacancy phases, can coexist.

A similar thermodynamic representation of the regions of the curve of $F(v)$ in Fig. 10 makes it possible to put them in correspondence to the following strain and fracture regions of the loaded solid: v_{-1}–v_1 is the region of elastic compression-tension of the equilibrium crystal; v_1–v_4 is the region of plastic strain of the solid without destruction of the imperfect material and without the possibility of its return to the equilibrium state (for example, during annealing); v_4–v_6 is the region of discontinuities of various scale (micropores, defects) in which viscous flow and material sublimation in the solid state are possible; $v < v_{-1}$ is the region corresponding to hydrostatic compression and characterized by incompressibility of the solid.

According to [1], in a dislocation nucleus in an equilibrium crystal there are a molar volume minimum $v_1 > v_0$ and a local minimum of $F(v_1)$. The smallest minimum $F(v_0)$ corresponds to a thermodynamically stable crystal with ideal translation invariance. Nanostructural states in a nanoinclusion are characterized by near-zero values of $F(v)$ (region I in Fig. 10). Region I corresponds to a strongly nonequilibrium transition state in which nanocrystals with a molar volume v_4 are surrounded by a structurally-indistinct shell with molar volume $v = v_5$. A dislocation will bend around a nanoparticle with a large elastic modulus, resulting in strengthening according to the Orovan model (Fig. 11a). However, material strengthening can also be caused by passage of a dislocation through a soft nanoparticle. When a dislocation passes through a nanoparticle with a small elastic modulus (Fig. 11b), the dislocation nucleus is split over the entire volume of the nanoinclusion, resulting in a significant decrease in its nonequilibrium relative to the state of the material of the soft nanoparticles and transition to a metastable state. To eliminate the blocking that arises in this case, the dislocation needs the additional stress [17]

$$\tau = (\gamma_{\mathrm{m}} - \gamma_{\mathrm{n}})/b + (\tau_{\mathrm{f},m} + \tau_{\mathrm{f},n})/2 + (\tau^*_{\mathrm{m}} + \tau^*_{\mathrm{n}})/2.$$

Here τ^*_{m} and τ^*_{n} is the short-range order fracture stress in the metal of the matrix and nanoinclusion, respectively; γ_{m} and γ_{n} are the energies of the packing defect, and $\tau_{\mathrm{f},m}$ and $\tau_{\mathrm{f},n}$ are the friction force of partial dislocations; b is the Burgers vector.

If a dislocation passes through a nanopore, a distinct threshold arises in the latter which slows the dislocation motion, leading to material strengthening. However, significant strengthening can be achieved only in nanostructural

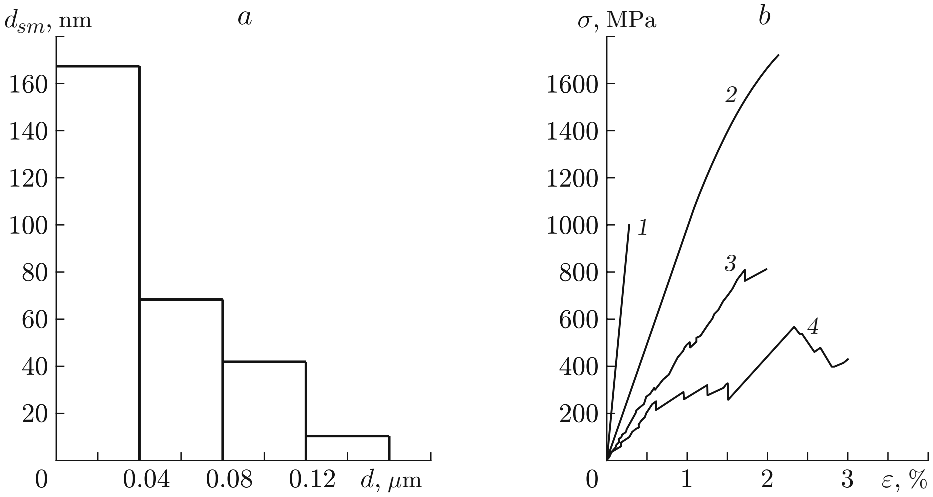

Fig. 12. Distribution of the submicropore size d_{sm} versus grain size d (a) and strain diagram (b) during compression of ZrO_2 ceramics: nonporous material (1) and $s = 2$ (2), 15 (3), and 26% (4).

materials in which high concentration of nanopores is possible. From Fig. 10, it follows that nanopores can be in equilibrium only with nanocrystals. In the present work, this conclusion was confirmed for nanostructural ceramics in which microcracks develop.

3. STRENGTHENING BY NANOPORES

It is known that the stress concentration near a cut in a solid is influenced by only two geometrical parameters: the length of the cut in a direction perpendicular to the tension axis and the minimum radius of curvature at the end of the cut along this direction [18]. A large pore in a solid acts a strong stress concentrator since it has an irregular geometrical shape with local curvature radii much smaller than the size of the pore. Materials with high porosity contain a large number of large pores promoting strong softening. Brittle materials, for example, porous ceramics have especially low strength properties [19].

A nanopore is an inclusion with curvature radius commensurable with the size of the nanopore, i.e., its shape is nearly spherical. Stress concentration in a low-porosity material does not play a determining role in its deformation softening. Of significance for material softening is the fact that, in the nanosize range, the boundary of the structural element is indistinct. A nanopore is an inclusion whose Young modulus is equal to zero. Therefore, the reduction in stress concentration should occur more rapidly with decreasing pore size than with decreasing Young modulus.

At the same time, in brittle ceramics, the life and ultimate strength are determined by the initiation and distribution of microcracks rather than by dislocation mechanisms. The strengthening role of nanopores in ceramics is that nanopores effectively impede the propagation and development of microcracks. This conclusion is supported by experiments on dioxide zirconium ceramics. Measurements by scanning electron photomicrographs show that the mean size of submicropores decreases in proportion to an increase in the grain size in ceramics and ranges from 50 to 80 nm (Fig. 12a).

Figure 12b shows typical strain curves obtained during active compression of samples of nonporous material and ceramics with various volumes of pore space. Nonporous ceramics is deformed elastically to the value $\sigma = 1000$ MPa and undergoes brittle fracture at a strain of $\varepsilon \leqslant 0.2\%$ (curve 1). The strain diagrams of ceramics with nanopores ($\varepsilon < 10\%$) are almost linear (curve 2). The slight deviation from a linear law at the top of the diagram is apparently due to the tetragonal-monoclinic phase transition under the action of stresses in the frontal region of the main crack characteristic of partially stabilized dioxide zirconium. A comparison of curves 1 and 2 shows that the presence of nanopores leads to a significant increase in the ultimate strength of the material (to a value $\sigma = 1700$ MPa) and to an order of magnitude increase in the strain margin before fracture ($\varepsilon = 2\%$).

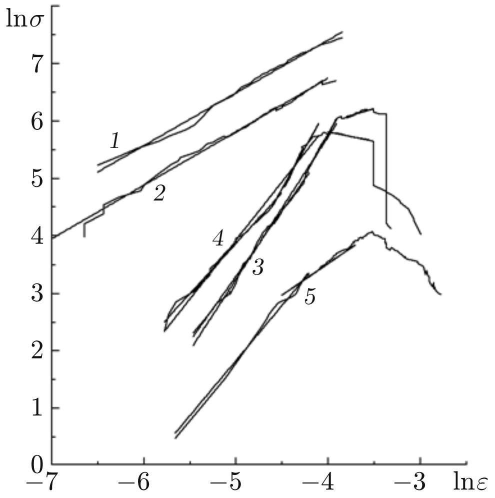

Fig. 13. Loading curves of ZrO_2 ceramics in double logarithmic coordinates for $s = 10$ (1), 15 (2), 23 (3), 29 (4), and 60% (5).

Increasing the volume fraction of porosity increases the variance of the pore size distribution. Both large and small pores are formed. A sharp decrease in the ultimate strength of the material is observed. The loading curves become more complex: the diagrams have regions of elastic deformation and failure of stress (curves 3 and 4 in Fig. 12b). The value of stress reduction and the extent of the sawtooth regions increase with increasing volume of the pore space in the material. The intermittent nature of stress–strain curves for high-porosity ceramics is due to local fracture processes. Each stress reduction is a consequence of the initiation and propagation of a microcrack in a local field. The subsequent stress growth indicates that in local volumes, the development of microcracks is impeded due to penetration of the crack mouth into the pore space.

From an analysis of the strain curves for porous ceramics given in Fig. 12b, it follows that their slope during active loading before the occurrence of nonlinear regions changes depending on the porosity value. The general form of these curves can be described by the power-law function $Y = bX^n$, where n is the parabolic index. Various deformation mechanisms determining the shape of the curve are possible, depending on the porosity: 1) purely elastic strain; in this case, the parabolic index of the strain curve is $n = 1$; the form of the function corresponds to Hooke law $\sigma = E\varepsilon$; 2) inelastic deformation (plasticity); in this case, $n < 1$; 3) deformation of the sample due to displacements of local volumes in these porous systems (pressing effect); in this case, $n > 1$. Generally, a superposition of all the above-mentioned mechanisms is possible.

The parabolic index can be found by plotting loading curves in double logarithmic coordinates and determining their slope (Fig. 13). In Fig. 13, it is evident that loading diagrams are converted to several straight-line segments with various values of n, and the higher the porosity, the larger number of linear segments can be distinguished. The indices n determined for most materials turned out to be larger than unity, and for some materials they reach large values $n = 8$. The presence of values $n > 1$ for small degrees of deformation, generally speaking, is unusual since fracture signs in such cases were not detected. Special metallographic studies of samples were performed under cyclic loading to small strains (until the occurrence of visible fracture signs). At this stage, the strain curve are reversible in strain because purely elastic deformation takes place. This is supported by the results of direct metallographic studies of materials: superimposition of photomicrographs of the structure of a material before compression loading and after unloading to the relative strain $\varepsilon = 1.5\%$ shows complete coincidence of the images. Thus, it can be argued that in the these materials, microfracture does not lead to irreversible displacement of fragments into the pore space.

An analysis of the strain diagrams shows that the presence of pores of various sizes has a significant effect on the mechanical behavior of the material. Figure 14 gives all index n in the strain equation measured from the slopes of the straight-line segments of the curves in Fig. 13 for compression of ceramics with submicropores versus total porosity. It is evident that the experimental values of n fall on three straight lines and that there is a critical value of the porosity for which the deformation of the porous solid changes significantly: the exponent of the power-law

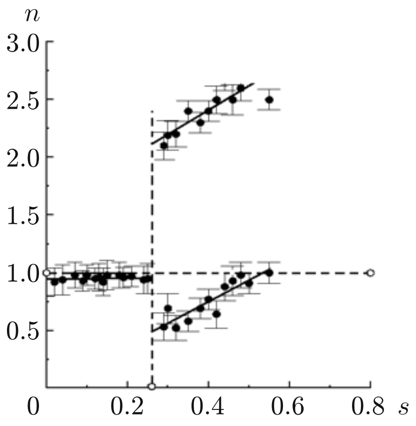

Fig. 14

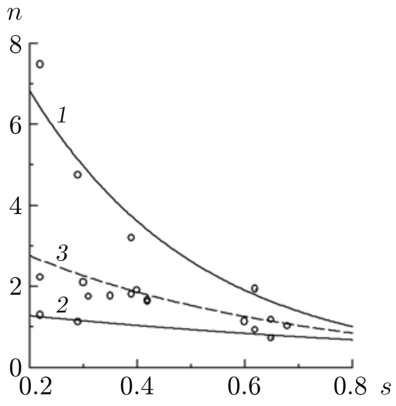

Fig. 15

Fig. 14. Parabolic index versus porosity for $ZrO_2(Y_2O_3)$ ceramics with submicron pore size.

Fig. 15. Parabolic index versus porosity for $ZrO_2(Y_2O_3)$ ceramics with macropores: boundaries of the range of values of n (1 and 2), averaged dependence $n(s)$ obtained for all experimental points (3).

function becomes much larger than that in the initial state. In this case, the material is actually divided into two subsystems which are differently deformed under external loading.

Materials with macroporosity have a different form of the dependence of n on porosity: the lower the porosity, the larger the exponent of the power-law function which decreases exponentially with increasing porosity (Fig. 15).

Simultaneous use of approaches of physical mesomechanics and nonequilibrium thermodynamics allows one to determine the positive effect of nanoporosity on the strength and fracture toughness of brittle nanostructural ceramics.

CONCLUSIONS

The mechanisms involved in the effect of nanosize inclusions, including nanopores, on the strengthening of solids are considered by simultaneously using of approaches of mesomechanics and nonequilibrium thermodynamics. Stress fields near inclusions and pores of various sizes are calculated. It is shown that any nanoinclusions are weak stress concentrators and cause material strengthening. The strengthening effect of nanopores is most significant for nanostructural materials.

This work was supported by Project of the Siberian Division of the Russian Academy of Sciences No. 3.6.1.1 and Russian Foundation for Basic Research Grant No. 10-08-01182-p, 09-01-00461).

REFERENCES

1. V. E. Panin and V. E. Egorushkin, “Physical mesomechanics and nonequilibrium thermodynamics as a methodological basis of nanomaterials science,” *Fiz. Mezomekh.*, **12**, No. 4, 7–26 (2009).
2. Ye. Ye. Deryugin, G. Lasko, and S. Schmauder, “Relaxation element method in mechanics of deformed solid,” in: W. U. Oster (ed.), *Computational Materials*, Nova Sci. Publ., New York (2009), pp. 479–545.
3. D. E. Eshelby, “Definition of the stress field, which was creating by elliptical inclusion,” *Proc. Roy. Soc. London, Ser. A*, **241**, No. 1226, 376 (1957).
4. J. Eshelby, *Continuum Theory of Dislocations* [Russian translation], Izd. Inostr. Lit., Moscow (1963).
5. G. Kirsch, “Die Theorie der Elastizitat und die Bedurfnisse der Festigkeitslehre,” *Zantralblatt Verlin Deutscher Ingenieure.*, No. 42, 797–807 (1898).
6. S. P. Timoshenko and J. N. Goodier, *Theory of Elasticity*, McGraw Hill, New York (1970).

7. H. G. Hahn, *Elastizitatstheory. Grundlagen der Linearen Theorie und Anwendungen*, Teubner, Stuttgart (1985).
8. N. I. Mushelišvili, *Some Basic Problems of the Mathematical Theory of Elasticity*, Noordhoff, Groningen (1953).
9. A. V. Mali and S. J. Singh, *Deformation of Elastic Solids*, Prentice Hall, New York (1992).
10. I. S. Grigor'ev and B. Z. Meilikhov, *Physical Quantities: Handbook* [in Russian], Énergoatomizdat, Moscow (1991).
11. A. P. Sutton and R. W. Balluffi, *Interfaces in Crystalline Materials*, Clarendon Press, Oxford (1995).
12. R. Z. Valiev and I. V. Aleksandrov, *Nanostructural Materials Produced by Intense Plastic Deformation* [in Russian], Logos, Moscow (2000).
13. M. Yu. Gutkin and I. A. Ovid'ko, *Defects and Plasticity Mechanisms in Nanostructural and Noncrystalline Materials* [in Russian], Yanus, St. Petersburg (2001).
14. H. S. Nalwa (ed.), *Handbook of Nanostructured Materials and Nanotechnology*, Vols. 1–5, Academic Press, San Diego (1999).
15. H. Gleiter, "Nanostructured materials: Basic concepts and microstructure," *Acta Mater.*, **48**, No. 1, 1–29 (2000).
16. H. G. Van Buren, *Imperfections in Crystals*, North-Holland, Amsterdam (1960).
17. V. E. Panin, E. F. Dudarev, and L. S. Bushnev, *Structure and Mechanical Properties of Solid Substitution Solutions* [in Russian], Metallurgiya, Moscow (2009).
18. A. Thompson, "Substructure strengthening mechanisms," *Met. Trans.*, No. 6, 833–842 (1977).
19. S. N. Kul'kov and S. P. Buyakova, "Phase composition and features of structure formation in nanocrystalline ZrO_2," *Ros. Nanotekhnol.*, No. 1, 119–132 (2007).